Water entry of cups and disks

Jesse Belden[1,†], Nathan B. Speirs[1], Aren M. Hellum[1], Matthew Jones[2], Anthony J. Paolero[1] and Tadd T. Truscott[3]

[1]Naval Undersea Warfare Center Division Newport, 1176 Howell Street, Newport, RI 02841, USA

[2]Department of Mechanical and Aerospace Engineering, Utah State University, Logan, UT 84322, USA

[3]Division of Physical Sciences and Engineering, King Abdullah University of Science and Technology (KAUST), Thuwal 23955-6900, Saudi Arabia

It is known that the water entry of a body with a recessed, cupped nose can suppress the splash and air cavity typically observed for solid body entry (Mathai, Govardhan & Arakeri, *Appl. Phys. Lett.*, vol. 106, 2015, 064101). However, the interplay between the captive gas in the cup, the cavity and the splash is quite subtle and has not been thoroughly explored. Here we study the cavity and splash dynamics associated with the vertical water entry of cups and find a variety of regimes over a range of Weber numbers (We_D) and dimensionless cup depths. Our parameter space spans a transition between slow-developing cavities with long closure times (low We_D) to fast-sealing cavities (high We_D). An important dynamic event is the evacuation of trapped gas from within the cup, which drives the ensuing cavity and splash behaviour. Through modelling, we predict the conditions for which the evacuating gas inflates a cavity that opens to the atmosphere versus inflating a submerged cavity that suppresses air entrainment from above the surface. We also compare our cup water entry findings to the impact phenomena observed for flat disks, which entrap gas on the front surface similar to cups. In doing so, we reveal the sensitivity of disk splash and cavity behaviour to impact angle, and show that disks share a common regime with cups, in which a thin splash quickly seals on the body. We deduce the mechanisms by which increasing cup depth delays the cavity seal time in this regime. These findings reveal that cups may in fact promote or suppress cavity growth, depending on the cup depth and impact conditions.

Key words: cavitation

† Email address for correspondence: jesse.l.belden2.civ@us.navy.mil

1. Introduction

A body entering the water often creates an air-filled cavity below the surface and a splash above. While details of the splash and cavity can vary for bodies of different shape, size, speed and surface properties, certain characteristics are ubiquitous. The richness of the physics, along with the range of applications in water entry have garnered significant research attention (Truscott, Epps & Belden 2014). Much of the previous work has focused on bodies with convex, flat or conical nose shapes. Here we investigate how bodies with recessed noses dramatically alter the typical cavity and splash formations by studying the vertical water entry of cylindrical cups and disks.

Nose shapes with sharp changes in curvature, such as disks (Bergmann *et al.* 2009) and vertical cylinders (Duclaux *et al.* 2007; Bodily, Carlson & Truscott 2014), readily form splashes and cavities. In the case of sphere impact, cavity and splash features depend on the static wetting angle of the material θ, the Weber number $We_D = \rho D U^2 / \sigma$ and the Froude number $Fr = U^2 / gD$, where U is the impact velocity, ρ the liquid density, σ the surface tension, g is gravity and D is a length scale. For spheres, D is the sphere diameter; for the cups in this paper, D is the cross-sectional diameter of the body. Duez *et al.* (2007) showed that spheres impacting with sufficiently large We_D form cavities when the splash separates from the body, with the critical value of impact velocity for cavity formation being a function of θ. Below this velocity, they found that the splash remains attached to the sphere throughout impact, preventing the air entrainment required for cavity formation. Similar cavity phenomena have been observed for slender bodies with ellipsoidal or ogival nose shapes (May 1975; Bodily *et al.* 2014). Speirs *et al.* (2019) later expanded this work, showing that below a certain We_D, cavities can again form because no splash is generated.

When the conditions for cavity formation are met, the cavity grows underwater drawing in air from above the surface until a sealing event closes the cavity. Cavities are typically classified into one of four regimes defined by Aristoff & Bush (2009), which are distinguished by the spatial location of the seal event. We concern ourselves here with deep seal and surface seal cavity types, which occur for a wide range of nose geometries. In a deep seal, the cavity pinches off below the surface with the above surface splash crown forming an aperture open to air. However, a surface seal closes off the cavity from the air above when the splash crown domes over on itself above the surface (Gilbarg & Anderson 1948; May 1975; Mansoor *et al.* 2014; Marston *et al.* 2016; Eshraghi, Jung & Vlachos 2020). In the defining work of Aristoff & Bush (2009), the seal location is well removed from the spherical body for deep and surface seals. However, it is also possible that the axial extent of the body is such that the seal point lands on the body. In this case, the deep and surface closure phenomena still occur, except the sealing event is marked by contact of the cavity or splash with the body (e.g. figure 1*a*,*b*). Bodily *et al.* (2014) showed this for long slender bodies (with length to diameter $L/D = 10$) for a variety of convex and disk nose shapes. Regardless of the extent of the body, the water entry phenomena at early times (i.e. small submergence) are a function of the nose geometry and not the body length.

The axial extent of the body need not be large to get 'on body' seal when the impacting nose is cupped or concave. Mathai, Govardhan & Arakeri (2015) showed that a concave nose can stunt cavity development, observing a gas torus that surrounds the outer circumference of the body shortly after impact, which we reproduced with our cups (figure 1*c*). They reported no evidence of splash formation and no clear cavity emanating from the nose. Here we vary the impact speed U and cup depth h and find a wide range of behaviours, including many in which a splash and clear cavity are indeed formed. Using both experiments and theory, we show how the behaviour of the air initially trapped in the
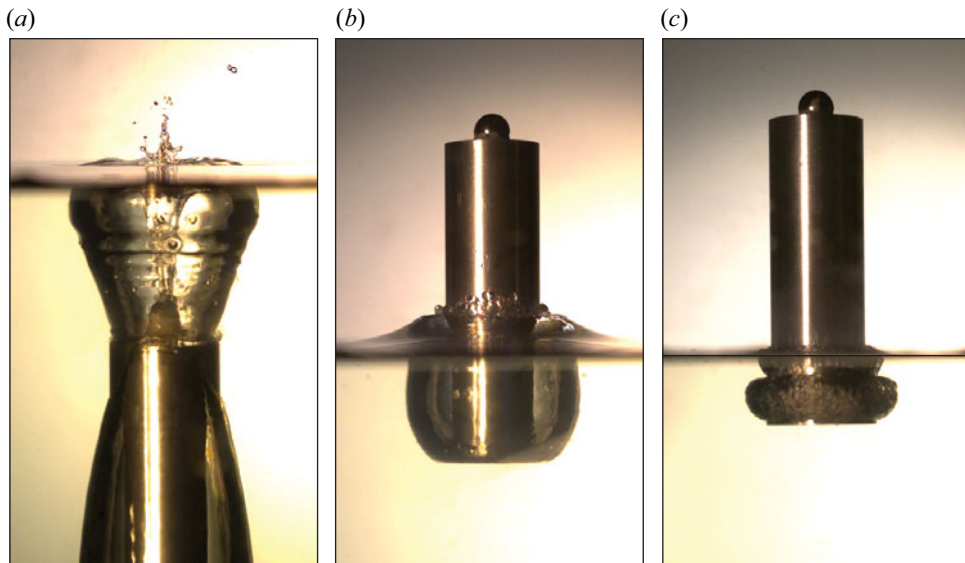
Figure 1. Three different regimes of cup water entry, all shown at the moment of cavity seal. (*a*) A cup at low impact speed produces a large cavity that ultimately closes in a deep seal on the body below the surface ($h/D = 0.16$, $We_D = 689$). (*b*) The same cup at slightly higher speed produces an above-surface seal in which the splash rim closes on the body above the surface ($h/D = 0.16$, $We_D = 710$). (*c*) A deeper cup at higher impact speed produces a closed torus cavity that does not open to the atmosphere and is filled by gas that escapes from the cup ($h/D = 0.63$, $We_D = 2390$).

cup affects splash and cavity formation. Varying the initial volume of trapped gas (via cup depth) introduces a time scale for gas evacuation that has a non-monotonic dependence on We_D, which we rationalize with theory. For high We_D, cup entry phenomena are inertia dominated and we find cup depth h to be the dominant length scale determining this gas evacuation time. For low We_D, we find the width of the cup lip to be a relevant length scale in distinguishing cavity closure phenomena as surface tension becomes important. The effect of these parameters on the resulting cavity formation, splash characteristics and cavity seal are captured in regime diagrams. A region of the regime diagram contains the closed torus case described by Mathai *et al.* (2015), for which cavity development is suppressed. Cavity forming cases are characterized by the seal time t_{cs}, which we find to be significantly affected by h for large We_D. We place our results in context of water impacts of cylindrical bodies with a flat disk nose shape which also trap air beneath the nose, although the volume and evacuation time scale, as described by Jain *et al.* (2021*a*), are much smaller than for our cups. Thus, our results generally extend the understanding of the effect of air entrapment beneath solid bodies entering water.

2. Experimental set-up

Figure 2 shows the experimental set-up used in this study in which thin-walled cups are dropped from an electromagnet into a tank of water. The cups are made from an aluminium cylinder with length $L = 100$ mm, cross-sectional diameter $D = 25.4$ mm and cup depths of $h = 1, 3, 4, 8, 16$ and 25.4 mm. The mass is varied between 94 and 119 g. The recessed cup is machined such that the interior walls form a thin wedge with an angle of $\beta \approx 10°$ and the lip of the cup has radius r, which for the cups listed above are $r = 0.1, 0.1,$
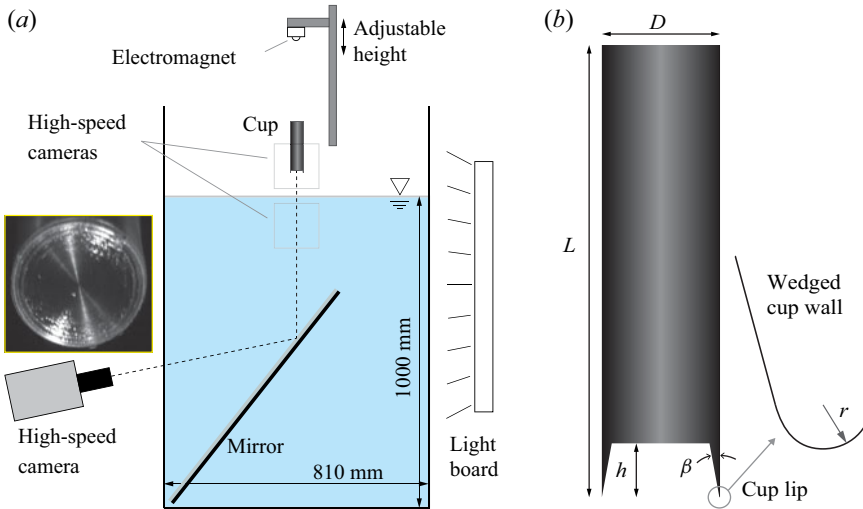
Figure 2. (*a*) Experimental set-up with three high-speed cameras viewing the water entry event. The inset image shows a high-speed camera viewing beneath the impact via a mirror placed in the tank. (*b*) Thin-walled cups are made by cutting a recess in a cylinder to depth *h*; the thin walls of the cup form a wedge angle $\beta \approx 10°$, and the lip of the cup has radius *r*.

0.09, 0.22, 0.11 and 0.07 mm. Additionally, an identical cylinder with a flat disk nose was machined and tested at each impact condition; we refer to this body as the 'disk' throughout the paper. A ball bearing affixed to the top of the cylinder creates a single point of contact with the electromagnet. The height of the electromagnet controls the impact velocity of the cups *U*, which is varied from 0.68 to 5.9 m s^{-1}, yielding a Weber number range of $We_D = 1.17 \times 10^2$ to 1.23×10^4.

High-speed videos below and above the surface are used to interrogate properties of the cavity and splash, respectively, at frame rates between 4000 and 50 000 frames s^{-1}. From the camera images, we measure several time scales described in § 3. The experiment is designed such that the cups fall freely; therefore, the angle α between the impacting face and the water surface may be non-zero upon water impact. We measure this angle from the third high-speed camera, which is aimed at an angled mirror in the tank to enable viewing of the impact from below (sample image shown in figure 2*a*). The angle is measured as $\alpha = \sin^{-1}(U\Delta t_\alpha/D)$, where Δt_α is the time difference between the moment of first contact and when the full perimeter of the cup lip comes in contact with the water. For the cup cases reported herein, the mean and standard deviation of α is 0.25° and ±0.21°, respectively, except for the data reported in Appendix A, wherein we investigate the effect of larger α, up to approximately 1°. For the disk, we hold a tighter tolerance on α, as discussed in § 5.

3. Cavity and splash behaviour

Figure 1(*c*) shows a phenomenon similar to that shown by Mathai *et al.* (2015), in which a torus of gas emanates from the cup nose and no splash is apparent above the surface. However, unlike the findings of Mathai *et al.* (2015), we find other conditions for which the cavities reopen to the air above and expand to varying degrees, before sealing on the body. These various regimes depend on the sequence of a common set of underlying phenomena, which we summarize here and then expand upon later. As the wedged cup
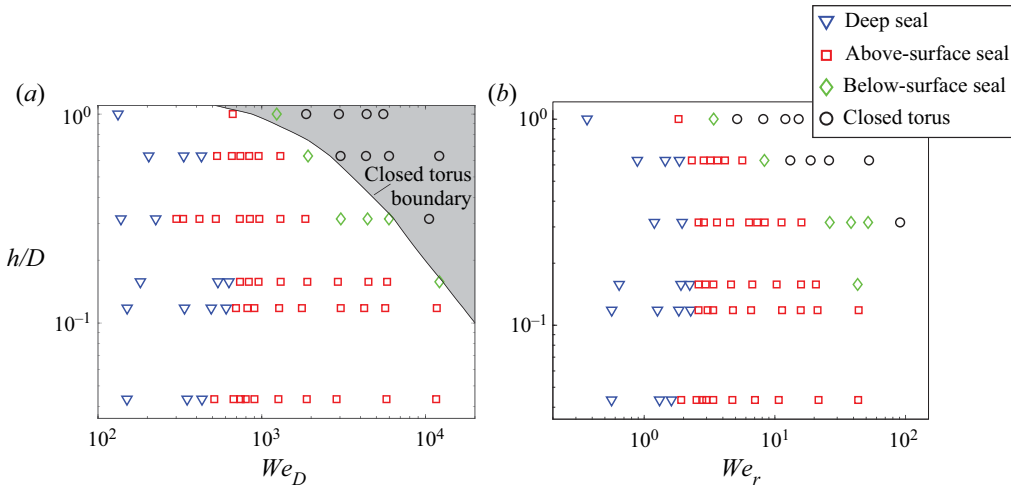
963 A14-4

Figure 3. (*a*) Cavity and splash regimes for the water entry of cups over a range of h/D and We_D. The closed torus boundary is predicted by the model in §4.2. (*b*) Rescaling the data with We_r aligns the transitions between the low-Weber deep seal and above-surface seal regimes across cup depths.

wall impacts the free surface, water separates forming a small cavity around the cup that may imminently close on the body in a deep-seal like manner. As the cup descends, gas from inside the cup leaks out, which may or may not reopen the wedge cavity. The splash crown formed above the surface rises from the impact inertia, and is further displaced upwards by the gas escaping the cup, which inflates the cavity below the surface and pushes the free surface upwards. The splash can be observed to close on the body, reopen again and then close again as the final seal. While the above-described events generally persist across our experimental parameter space of We_D and h/D, we find a wide range in the cavity and splash behaviour. We classify these behaviours into four regimes – deep seal, above-surface seal, below-surface seal and closed torus – which are plotted in the diagrams shown in figure 3. Representative cases of each regime are shown in figures 4 and 5, and see supplementary movies 1–5 available at https://doi.org/10.1017/jfm.2023.330.

At the lowest speeds with $We_D \approx 100$–600, a large cavity is formed and fed by the air above the surface until ultimately closing on the body well below the surface in a deep seal type event (e.g. figure 4*a*, $h/D = 0.04$, $We_D = 151$; supplementary movie 1). The cavity remains open to air prior to this deep seal and a short, thick rim dominated by surface tension is formed upon water impact. Gas from inside the cup escapes into the growing cavity, but we find no evidence that the escaping gas has a significant effect on the rim or cavity development in the deep seal regime, as it does in other regimes. The rim lacks sufficient inertia to form the thin ejecta film known as the splash crown, and never seals on the body. This lack of the thin ejecta film is expected for low We_D as Speirs *et al.* (2019) observed the same for sphere water entry below a critical Weber number of $We_D \approx 240$.

Traversing up and right on the regime diagram of figure 3(*a*), we find the above-surface seal behaviour shown in figure 4(*b*) ($h/D = 0.16$, $We_D = 1016$; supplementary movie 2). The higher inertia forms a thinner ejecta sheet which has the hallmark rim and crown ($t = 10.3$ ms) (Yarin 2006; Zhang *et al.* 2012). The rim initially moves up and radially outwards before beginning to move radially inwards at $t \approx 20$ ms. Meanwhile, the expanding cavity (from inflowing air and gas escaping from the cup) pushes up the free surface, forming a
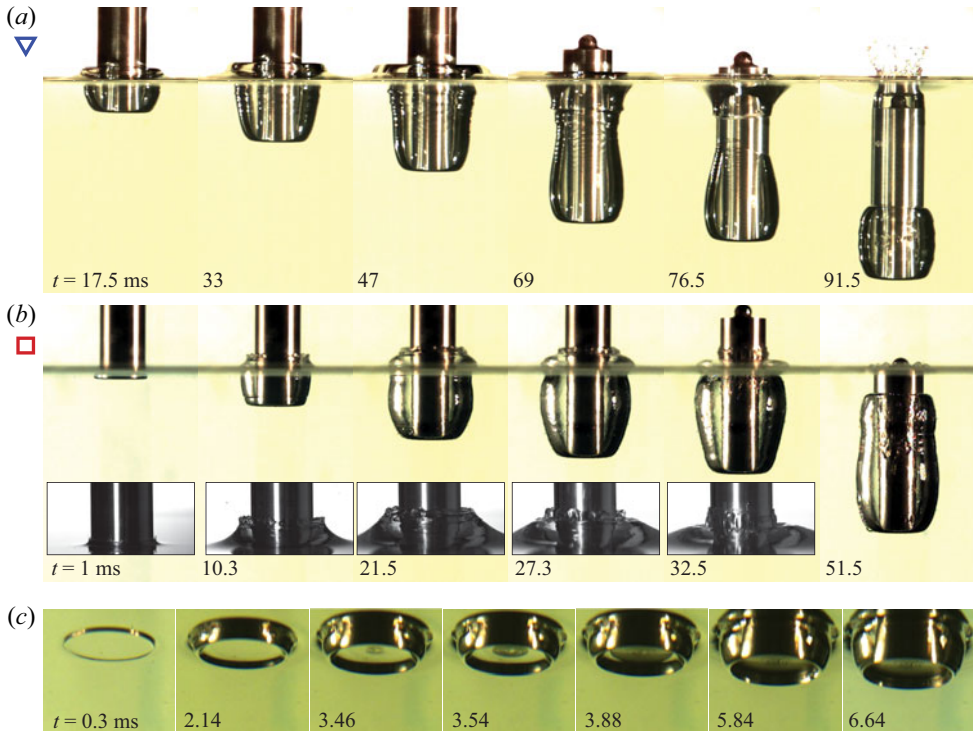
Figure 4. Image sequences of low-We_D cup water entry behaviour. (*a*) In the deep seal regime, the cavity closes on the body beneath the water surface and no splash sheet is formed ($h/D = 0.04$, $We_D = 151$). (*b*) In the above-surface seal regime, a splash sheet is formed and the cavity is sealed when the kink between the rim and sheet pinches in on the body above the surface at time $t = 32.5$ ms ($h/D = 0.16$, $We_D = 1016$; inset shows above surface camera view). These cases are shown in supplementary movies 1 and 2. (*c*) A below-surface camera view reveals the cup gas behaviour that is typical of low-We_D impacts ($h/D = 0.12$, $We_D = 562$). The internal gas–liquid interface moves up, compressing the gas in the cup and forming a meniscus at the cup lip ($t = 2.14$ ms). The interface then de-wets on the inside face of the cup ($t = 3.46$ ms), the contact line retracts to the inner walls ($t = 3.46$–5.84 ms) and then recedes to the cup lip ($t = 6.64$ ms), thus completing the gas evacuation process (see also supplementary movie 6).

region of sharp curvature between the ejecta sheet and the rim ($t = 27.3$ ms). This kinked region then moves rapidly in towards the body, sealing at $t = 32.5$ ms. The phenomenon of the splash rim drawing radially inwards occurs for surface seal events in sphere water entry (Gilbarg & Anderson 1948; Marston *et al.* 2016; Eshraghi *et al.* 2020), where surface tension forces and an air-flow-induced pressure difference across the sheet pull the rim inwards. Herein, the rim closes on the body, sealing the cavity from further expansion.

The internal cup gas behaviour that is characteristic of lower We_D impacts is shown in figure 4(*c*) ($h/D = 0.12$, $We_D = 562$). Upon impact, the wedge cavity is seen forming around the outside of the cup ($t = 0.3$ ms). The internal gas–liquid interface moves up relative to the leading edge, compressing the cup gas and forming a meniscus at the lip ($t = 2.14$ ms). Gas begins escaping from the cup in a thin axisymmetric film, as evidenced by waves emanating from the cup lip (supplementary movie 6). The interface then de-wets on the inside face of the cup ($t = 3.46$ ms), the contact line retracts to the inner walls ($t = 3.46$–5.84 ms) and then recedes to the cup lip ($t = 6.64$ ms), thus completing the gas evacuation process.
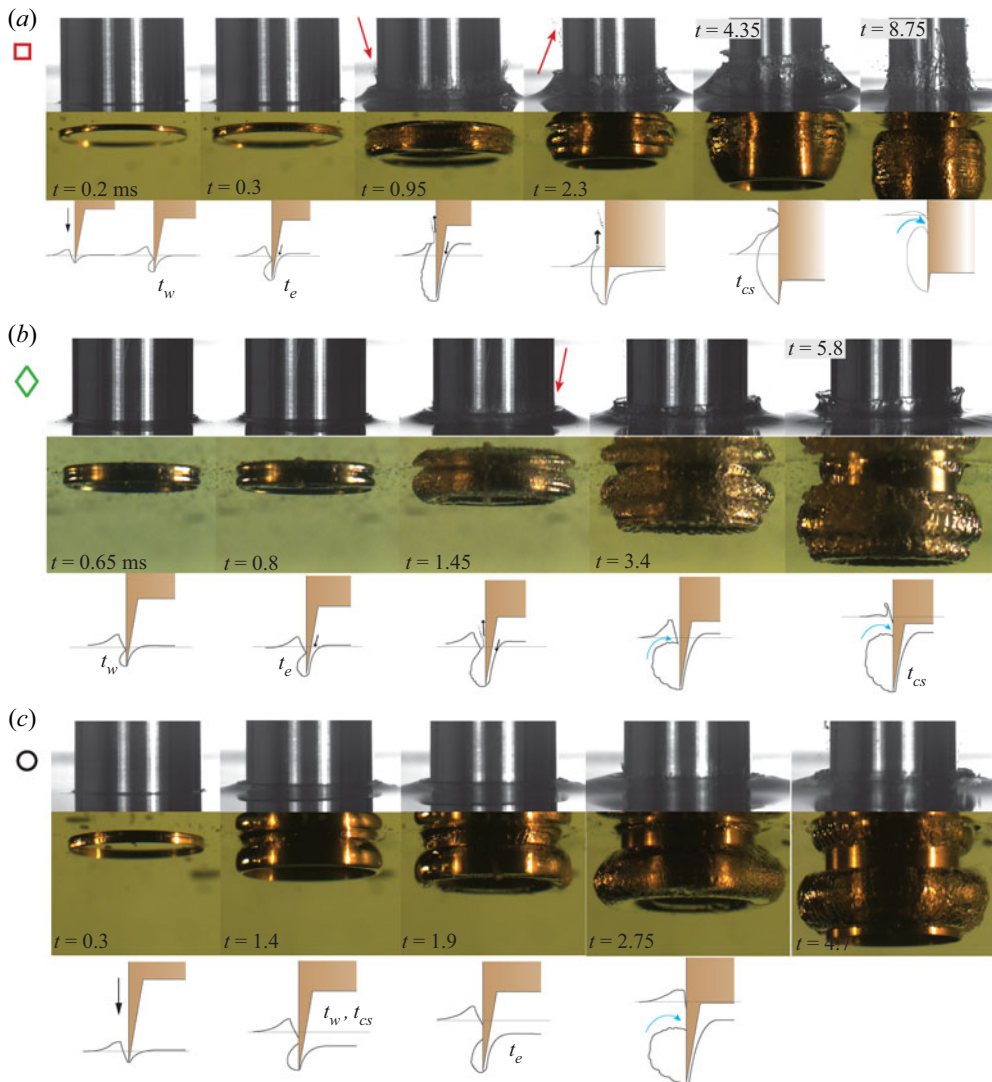
963 A14-6

Figure 5. Image sequences and schematics of high We_D cup water entry regimes. (*a*) In the above-surface seal regime, escaping gas reopens the wedge cavity and drives the splash sheet and a high-speed spray up from the surface (red arrows). The splash rim seals on the body, and then the water flow recirculates around the toroidal cavity (blue arrows), pulling flow down along the body ($h/D = 0.16$, $We_D = 2808$). (*b*) For a below-surface seal, the gas escapes late relative to the entry time and barely reopens the wedge cavity to the atmosphere ($h/D = 0.32$, $We = 2852$). (*c*) In the closed torus regime, the gas escapes from the cup so late that the cavity never reopens to the air above ($h/D = 0.63$, $We = 5806$). The wedge seal time, gas escape time and cavity seal time are denoted as t_w, t_e and t_{cs}, respectively. These cases are shown in supplementary movies 3–5.

Increasing We_D for the same cup depth, as shown in figure 4(*b*), yields the behaviour shown in figure 5(*a*) ($h/D = 0.16$, $We_D = 2808$; supplementary movie 3). This case still falls in the above-surface seal regime, but the seal time on the body is an order of magnitude faster than the case shown in figure 4(*b*). At this higher impact speed, the gas evacuation from the cup becomes much more evident in the roughening of the cavity interface ($t = 0.95$ ms); gas first begins escaping the cup at the escape time $t_e = 0.3$ ms, which is after the wedge seal has occurred. The escape time t_e is determined from

high-speed images from the below water camera, and is evidenced by waves emanating from the cup lip and a subsequent rapid expansion of the cavity. As the gas evacuates, it drives the wedge seal contact line up and away from the body, ejecting a thin liquid sheet and high-speed spray upwards (indicated by arrows at $t = 0.95$–2.3 ms). Next, the thin sheet contacts the body and quickly ruptures, reopening the cavity to the air above ($t = 0.95$ ms). In contrast to the lower We_D case, the splash rim diameter is smaller and does not deviate as far radially outwards from the body ($t = 2.3$ ms). The inflating cavity again deforms the splash sheet by pushing up the free surface and the rim seals on the body at $t_{cs} = 4.35$ ms. This is the third and final time that the cavity seals (wedge seal, thin sheet seal and splash rim seal), but this time it does not reopen. After sealing, as the cavity pulls away from the surface, the liquid flow recirculates around the toroidal cavity, resulting in a depression of the free surface ($t = 8.75$ ms). Evidently, the combination of body inertia and gas flow have a significant effect on the splash development and cavity seal in this regime.

Keeping We_D constant and increasing the cup depth to $h/D = 0.32$ yields the regime we call below-surface seal shown in figure 5(*b*) ($h/D = 0.32$, $We = 2852$; supplementary movie 4). The wedge cavity seal is more obvious in this case ($t_w = 0.65$ ms). Furthermore, the time scale for gas escape ($t_e = 0.8$ ms) is longer than in the case shown in figure 5(*a*). While the cavity does reopen to air above, as evidenced by ejected spray (red arrow at $t = 1.45$ ms), the recirculating flow around the gas toroid acts quickly to reseal the cavity on the body below the surface and above the toroid (blue arrows in figure 5*b*). As a result, the final sealed cavity volume is much smaller than for previous regimes, despite having a larger initial volume of gas trapped in the cup.

Finally, in the upper right portion of the regime diagram (figure 3*a*), we find the closed torus behaviour shown in figure 5(*c*) ($h/D = 0.63$, $We = 5806$). A very pronounced wedge cavity forms upon impact, seals on the body ($t_w = 1.4$ ms) and pulls away from the surface, all before gas begins evacuating from the cup at $t_e = 1.9$ ms. Here, the gas begins escaping the cup through irregular bubbles before evacuating axisymmetrically around the cup lip ($t = 2.75$ ms). By the time the gas begins to escape, the cup has already submerged to the point where the cavity never reopens to the air above. As the cup continues to descend, a depression in the surface gets pulled down along the body, but does not reconnect to the toroidal cavity ($t = 4.7$ ms; see also supplementary movie 5). Thus, the only and final cavity seal occurs at the moment of wedge cavity closure. In this regime, the entire contents of the toroidal cavity are the gas initially trapped in the cup and the air entrained into the wedge cavity. It is also worth noting that the closed torus case shown in Mathai *et al.* (2015) for a concave hemispherical nose has parameters ($We_D = 2.81 \times 10^4$ and $h/D = 0.67$) that place it in the closed torus regime on our regime diagram (figure 3*a*). In contrast to the two intermediate regimes, for which a splash rim and sheet are prominent features, no discernible splash sheet is observed in the closed torus regime. Positing that the dominate splash formation mechanism for closed torus cases is the water entry of the wedged cup walls, we suggest computing the Weber number with the cup lip radius r, $We_r = \rho r U^2 / \sigma$. Calculating this for the closed torus cases gives the range $We_r \approx 10$–200, where we might reasonably expect surface tension to significantly affect the splash development (or lack thereof, Speirs *et al.* 2019). Furthermore, our $h/D = 0.32$ cup was machined with r approximately two times larger than the other cups. Rescaling with We_r aligns the transition between the low-We_D deep seal and above-surface seal regimes on the diagram (figure 3*b*).

The closed torus cases are further evidence that the evacuation of gas from the cup is the driving factor in the splash and cavity dynamics for regimes in which the cavity is
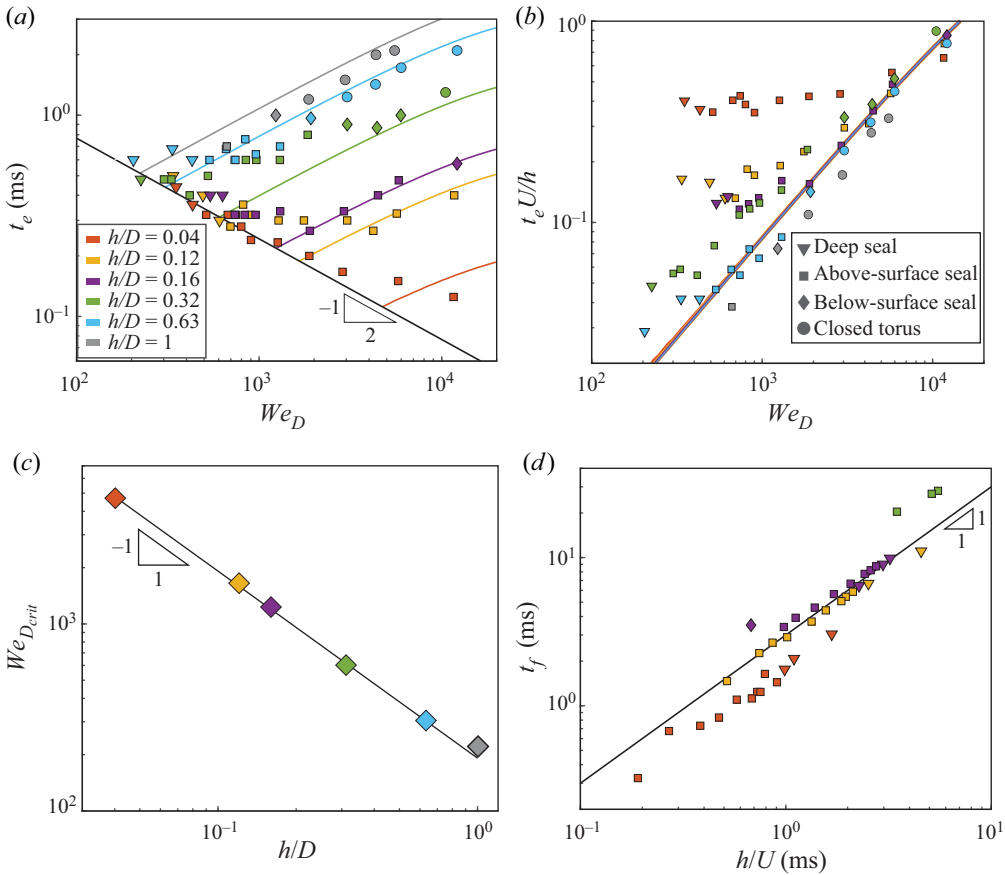
963 A14-8

Figure 6. (*a*) Gas escape time t_e as a function of We_D. The separate colour curves come from the high-We_D model in §4.2. The black curve, $t_e \propto We_D^{-1/2}$, comes from the low-We_D scaling analysis of §4.3 with $\kappa_l = 1.1(10^{-3})$. (*b*) Normalizing the escape time as $t_e U/h$ compresses the behaviour at high We_D towards a single curve. The experimental data for each cup intersect this curve at different values of We_D, and then follow the collapsed model predictions. (*c*) The intersection between the low- and high-We_D model predictions occurs at $We_{D_{crit}} \propto (h/D)^{-1}$ (the proportionality constant for the curve on the plot is 190). (*d*) The total time required to finish evacuating all cup gas t_f scales linearly with h/U; the line passing through data points is $t = 3h/U$. For all plots, symbol colour indicates cup depth as shown in the legend in panel (*a*) and symbol shape indicates the cavity regime as indicated by the legend in panel (*b*).

reopened to the air above the surface. The experimental observations show the timing of gas escape to be crucial in determining if the cavity reopens or not. We thus turn our attention to modelling the trapped gas dynamics.

4. Cup gas behaviour

4.1. *Gas escape time*

We define the gas escape time t_e as the time from initial water impact to the first moment that gas begins to evacuate from the cup. Figure 6(*a*) shows experimental measurements of t_e as a function of We_D for each cup depth. The data show a non-monotonic dependence on We_D, with the escape time initially decreasing with increasing Weber number, before eventually beginning to increase as We_D increases. The critical We_D at which this trend
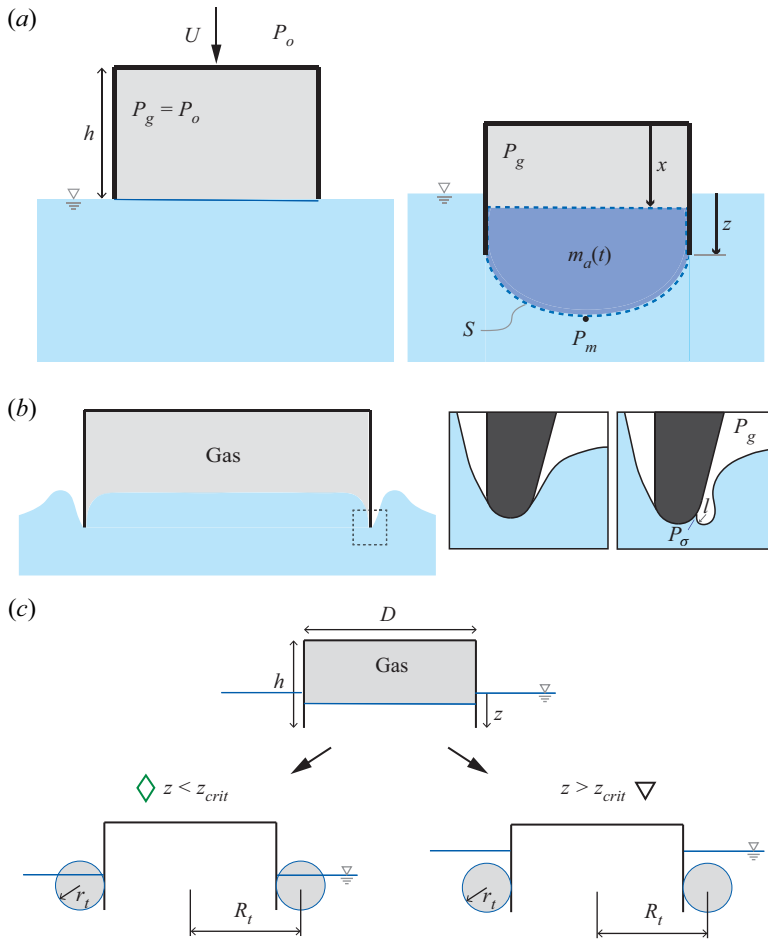
Figure 7. (*a*) High-We_D limit model as described in §4.2. The internal gas–liquid interface is assumed to have no curvature, which approximates the experimental behaviours seen at large We_D. We model the system as a two-body problem: one being the cup and the second the added fluid mass, which varies in time $m_a(t)$. (*b*) At low We_D, the model assumes a meniscus at the cup wall, characterized by radius l and Laplace pressure $P_\sigma = \sigma/l$. (*c*) Idealized model of the difference between the below-surface seal and closed torus regimes. If the cup has submerged beyond z_{crit}, then we expect that the gas torus will not reconnect to the free surface (i.e. closed torus regime).

change occurs is different for each cup depth. These diverging trends motivate different model constructs to capture the behaviour in each limit.

4.2. *High-We_D limit*

In the limit of high We_D, where inertia dominates surface tension, we suggest the idealized model depicted in figure 7(*a*). For high-We_D water impacts in general, the dominant force on the body during early times stems from the rate of change of added fluid momentum (Truscott *et al.* 2014). This added mass force F_m arises from the growing volume of liquid in the pool that must be accelerated from rest during early time after impact, and may be

963 A14-10

expressed as

$$F_m = -\frac{\mathrm{d}}{\mathrm{d}t}(m_a U_m),\tag{4.1}$$

where U_m is the instantaneous velocity of the added fluid mass, and m_a the added mass, which is a function of body geometry (Shiffman & Spencer 1945). For water entry problems, in which the geometry that has penetrated the surface is a function of time, the added mass is also a function of time, increasing from $m_a = 0$ just before impact to some maximum value at a later time. For cup impacts, we similarly expect the development of a transient added mass, which is driven by the motion of the body and the internal gas–liquid interface inside the cup.

Our model extends that of Bagnold (1939), who considered the compression of a gas by a liquid column inside a fixed cylinder. As depicted in figure 7(*a*), the internal gas–liquid interface is assumed to have no curvature and oscillates relative to the inside face of the cup through a displacement $x(t)$. Experimental observations at high We_D support this oscillatory model assumption during the initial gas compression phase (see supplementary movie 7). The position of the bottom of the cup relative to the nominal free surface is defined by $z(t)$. Neglecting drag on the cup lip, a force balance on the cup yields the equation of motion,

$$\ddot{z} = \frac{\pi R^2}{m}(P_o - P_g) + g,\tag{4.2}$$

where m is the cup mass, P_o the ambient (atmospheric) pressure and P_g the time-varying gas pressure in the cup. Assuming that the gas in the cup undergoes an adiabatic process such that PV^γ is constant, then the gas pressure in the cup can be written as $P_g = P_o h^\gamma x^{-\gamma}$, where $\gamma = 1.4$ is the adiabatic index for air. Substituting into (4.2) yields

$$\ddot{z} = \frac{\pi R^2}{m}P_o(1 - h^\gamma x^{-\gamma}) + g.\tag{4.3}$$

We next seek an equation of motion for the added fluid mass $m_a(t)$, which is assumed to move at uniform velocity $U_m(t) = \dot{z} + \dot{x}$. The rate of change of added fluid momentum is given by the force balance,

$$\frac{\mathrm{d}}{\mathrm{d}t}(m_a U_m) = P_g \pi R^2 - \int_S P_m \,\mathrm{d}S,\tag{4.4}$$

where S is the lower bounding surface of the added mass and P_m is the pressure on that surface (see figure 7a). As the depth z_m is small, we approximate $P_m \approx P_o$. Furthermore, though we do not know the exact geometry of surface S, we make the approximation $\int_S \mathrm{d}S \approx \pi R^2$. Applying these assumptions and expanding the left-hand side of (4.4) yields

$$m_a(\ddot{z} + \ddot{x}) + \frac{\mathrm{d}m_a}{\mathrm{d}t}(\dot{z} + \dot{x}) = \pi R^2 P_o(h^\gamma x^{-\gamma} - 1).\tag{4.5}$$

A first-order approximation for $m_a(t)$ is made by assuming a linear variation in time from $m_a(t = 0) = 0$ to m_a of a disk at some time t_m; that is, $m_a(t_m) = \frac{4}{3}\rho R^3$ (Jain, Vega-Martínez & Van Der Meer 2021b). As added mass is typically a function of normalized body submergence Ut/R, we assume $t_m \propto R/U = R/\kappa_m U$, where κ_m is a

963 A14-11

constant to be determined. Finally, we can write

$$\frac{\mathrm{d}m_a}{\mathrm{d}t} = \kappa_m \frac{4}{3}\rho R^2 U \qquad (4.6)$$

and

$$m_a = \kappa_m \frac{4}{3}\rho R^2 U t. \qquad (4.7)$$

Inserting (4.6) and (4.7) into (4.5) and solving for $\ddot{x}$ gives

$$\ddot{x} = -\ddot{z} - \frac{1}{t}(\dot{z} + \dot{x}) + \frac{1}{t}\frac{3\pi P_o}{4\kappa_m \rho U}(h^\gamma x^{-\gamma} - 1). \qquad (4.8)$$

The governing equations of motion (4.3) and (4.8) can be solved numerically to predict the time-varying motion of the gas-liquid interface inside the cup, with initial conditions: $z(t_0) = 0$, $\dot{z}(t_0) = U$, $x(t_0) = h$, $\dot{x}(t_0) = -U$. To avoid the singularity in (4.8) at $t = 0$, we begin the numerical integration at time $t_0 = 10^{-6}$ s, which is much smaller than the measured gas escape times. The model captures an oscillatory behaviour in which the cup gas compresses and then expands with decaying amplitude. Guided by observation, we assume the gas begins to leak out of the cup at the end of the first compression–expansion cycle. The period of this first cycle thus gives a prediction of the escape time t_e. A representative example of the predicted interface motion is shown in Appendix A.1.

The escape time t_e is computed using the above model for a range of h/D and We_D. The predictions of t_e against We_D in figure 6(a) (coloured lines) show good agreement with the experiments in the high-Weber limit, predicting both the rate of increase with We_D as well as the dependence on cup depth. We found the value of $\kappa_m = 0.8$ to give the best fit of the model to the data. Furthermore, when the escape time is normalized as $t_e U/h$, the model predictions collapse to a single curve (figure 6b). The experimental data for each cup intersect this curve at different values of We_D and then follow the collapsed model predictions. Prior to intersecting the common curves, $t_e U/h$ is roughly constant for each cup, which is consistent with the $t_e \sim We_D^{-1/2}$ trend in figure 6(a). The increase in escape time with increasing We_D is associated with a larger excursion of the interface, which then takes more time to expand back towards the cup lip. The collapse found with the scaling of $t_e U/h$ indicates that the gas escape process is dominated by inertia above the cup-depth-dependent critical We_D numbers.

4.3. *Low-We_D limit*

As We_D decreases, we expect that surface tension becomes increasingly important in the gas escape mechanism. High-speed video, such as that shown in figure 4(c) and supplementary movie 6, shows that the internal surface does not tend to oscillate at low We_D, rather it forms a meniscus at the cup wall, compresses the gas progressively and then de-wets from the cup centreline outwards. We hypothesize that the gas escape proceeds as shown in figure 7(b): as P_g increases the meniscus deforms, acquiring local radius l. The contact line will begin to move when the internal gas pressure overcomes the Laplace

pressure plus the local hydrostatic pressure, i.e. when

$$P_g > \frac{\sigma}{l} + P_o. \tag{4.9}$$

To estimate how the escape time scales at low We_D, we linearize $P_g = P_o h^\gamma x^{-\gamma}$ using a Taylor series expansion about $x = h$, giving

$$\begin{aligned} P_g &\approx P_g|_{x=h} + \left.\frac{\partial P_g}{\partial x}\right|_{x=h} (x - h) \\ &\approx P_o - \gamma P_o h^\gamma x^{-\gamma-1}|_{x=h}(x - h) \\ &\approx P_o \left[1 - \gamma \left(\frac{x}{h} - 1\right)\right]. \end{aligned} \tag{4.10}$$

Making the approximation $x \approx h - Ut$ and applying to (4.10) yields

$$P_g \approx P_o \left(1 + \gamma \frac{Ut}{h}\right). \tag{4.11}$$

Inserting this expression into (4.9) and solving for the corresponding escape time gives

$$t_e \approx \frac{h}{l} \frac{\sigma}{\gamma P_o U}. \tag{4.12}$$

Figure 6 shows that when following the low-We_D trend, the escape time data are not a function of h. Therefore, we conclude that $l = \kappa_l h \propto h$, where κ_l is an empirical constant, and rewrite (4.12) as

$$t_e \approx \frac{1}{\kappa_l} \frac{\sigma}{\gamma P_o U}. \tag{4.13}$$

The black line in figure 6(*a*) shows t_e from (4.13) with $\kappa_l = 1.1(10^{-3})$. This predicted trend of t_e shows good agreement with the low-We_D data for each cup. We also plot t_e versus U for only the low-We_D data in figure 13 of Appendix A, which highlights the weak dependence of t_e on h for a given speed.

The experimental data and our scaling analysis reveal that at low We_D, surface tension plays a significant role in the gas escape process, forming a meniscus as the gas–water interface deforms upon impact. Increasing impact inertia leads to reduced escape time, presumably by compressing the captured gas more quickly. At a critical Weber number $We_{D_{crit}}$, this trend reverses and t_e increases with increasing We_D. The data show that $We_{D_{crit}}$ is dependent on the cup depth. By finding the intersection points between the inertial model (Section 4.2) and the low-We_D scaling analysis, we find that $We_{D_{crit}} \propto (h/D)^{-1}$ as shown in figure 6(*c*).

4.4. *Closed torus regime*

Using our inertial model (§ 4.2), we can rationalize the boundary between open cavity cases and the closed torus regime on the regime diagram of figure 3(*a*). As the schematics and images of figure 5(*b,c*) show, the boundary hinges on whether the inflated toroid pushes the wedge seal contact line above the surface and away from the body. A simplified model of this behaviour, shown in figure 7(*c*), is used to predict this regime boundary. We first assume that all of the gas initially trapped inside the cup evacuates into a torus

with cross-sectional radius r_t and inner radius $R_t = r_t + D/2$. Note that in reality, the gas evacuation proceeds periodically over a number of cycles stemming from oscillations of the internal free surface. Nonetheless, observations show that the majority of the gas is evacuated in the first oscillation period. Equating the cup volume to torus volume gives $r_t^2(r_t + D/2) = D^2h/8\pi$, which can be solved numerically for r_t. For the cavity to remain sealed from air above as in the closed torus regime, we suggest that the cup must descend below a critical depth $z_{crit} = 2r_t$ such that the top of the torus is below the undisturbed free surface. Assuming constant speed over this descent yields a critical time scale $t_{crit} = 2r_t/U$. The time taken to inflate the gas torus must be longer than this critical time scale to observe the closed torus behaviour. Symbolically, $t_e + \tau > 2r_t/U$, where t_e is the escape time predicted by our inertial model and τ is the time required to inflate the torus after time t_e. Because the closed torus regime occurs for large We_D, the gas evacuation process should be dominated by inertia and it is thus assumed that $\tau = \kappa h/U$ (where κ is a constant). We find that the time required for all of the gas to finish evacuating follows this scaling, $t_f \propto h/U$ (see figure 6d), and thus expect the same scaling to hold for τ. The closed torus boundary curve plotted on figure 3(a) follows from conditions that satisfy

$$t_e + \kappa \frac{h}{U} = \frac{2r_t}{U}, \tag{4.14}$$

where $\kappa = 0.4$ is found empirically (see Appendix A.1 for details). Thus, our inertial model of the cup gas dynamics, coupled with an empirically motivated torus formation time predicts the boundary between the closed torus behaviour and the regimes in which the cavity reopens to air above the surface.

5. Disk water impact

We aim now to place the cup behaviour in the context of a canonical geometry by studying an identical cylindrical body, but with a flat disk nose ($h/D = 0$). Similar to cups, disks have also been shown to trap an air layer on the nose due to the deformation of the pool surface caused by the approach of the disk (Jain *et al.* 2021b). Yet, as disks do not have the wedge-shaped walls to contain this air layer, we find that the splash and cavity behaviour of disk impact is highly sensitive to the inclination angle of the face, α, relative to the flat free surface. Typically, past studies on the vertical water entry of disks have either actively enforced that the disk face impacts truly flat to the surface (Peters, van der Meer & Gordillo 2013; Jain *et al.* 2021a,b) or have explicitly varied the inclination angle, but for values of $\alpha \geq 2°$ (Bodily *et al.* 2014; Sun *et al.* 2021). Herein, we find that deviations of angle within the range $0° < \alpha \lesssim 1°$ are sufficient to change the time at which the splash seals on the body by an order of magnitude. This time, known as the cavity seal (or surface seal) time t_{cs}, is plotted in figure 8(a) against We_D for a range of $0° < \alpha \lesssim 1°$, for our disks. Figure 8(b) shows a corresponding regime diagram for the cavity closure type. At low $We_D \approx 100$, the cavity closes in a deep seal in the same manner as for the cups. As We_D increases, the seal time and regime both become sensitive to α. This is particularly evident for $We_D \approx 100$–400, where a deviation in α from $\approx 0.1° \rightarrow 0.5°$ can change the regime from above-surface seal to deep seal. Even if a difference in angle does not cause a regime change, it may still significantly affect the seal time and resulting cavity volume. The inset images in figure 8(a) show the cavities shortly after t_{cs} for two above-surface seal cases at the same We_D. The difference in angle ($\alpha = 0.145°$ versus $\alpha = 0.44°$) increases the seal time from $t_{cs} = 2.64$ to 15.68 ms.

963 A14-14
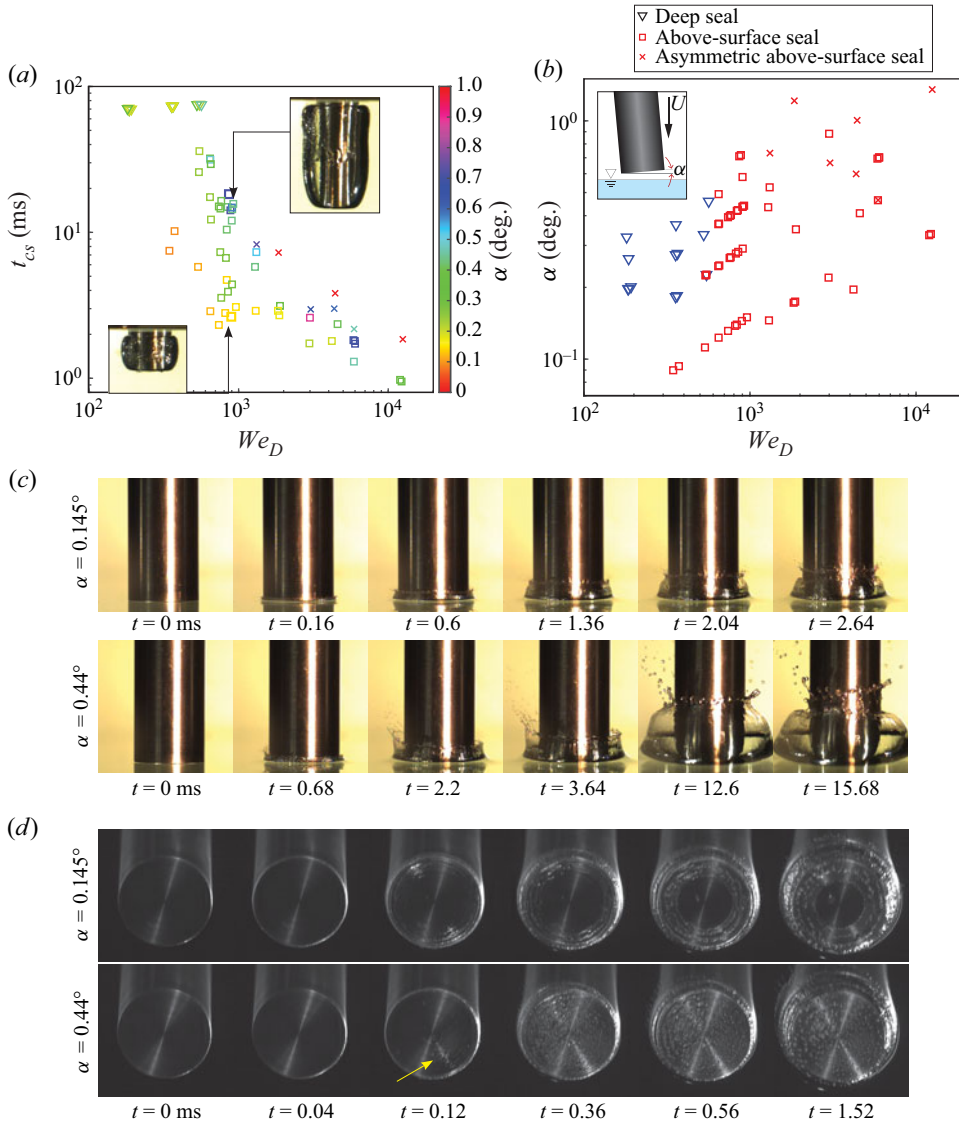
Figure 8. (*a*) Cavity seal time as a function of We_D for disk impacts at different angles of attack ($0° < \alpha < 1°$). The inset images show the difference in cavity size between a case with $\alpha = 0.145°$ and $\alpha = 0.44°$ (both at $We_D \approx 900$). (*b*) A diagram of α versus We_D shows how sensitive the regimes are to angle for disks. (*c*) Splash development and seal for disk impact with $\alpha = 0.145°$ (top) and $\alpha = 0.44°$ (bottom). (*d*) Below-surface views showing the breakdown of the entrapped air for disk impact with $\alpha = 0.145°$ (top) and $\alpha = 0.44°$ (bottom). The yellow arrow points out asymmetric wetting on the disk face. These two cases are shown in supplementary movies 8 and 9. The cases shown in panels (*c*) and (*d*) correspond to the inset images in panel (*a*).

Figure 8(*c*) shows the corresponding splash development for these two cases. For the nearly flat impact ($\alpha = 0.145°$), the splash rim is symmetric ($t = 0.6$ ms), does not deviate far from the body radially ($t = 1.36$–2.04 ms) and closes in on the body within a few milliseconds ($t = 2.64$ ms). For the inclined impact ($\alpha = 0.44°$), an asymmetric splash forms upon impact ($t = 0.68$–2.2 ms), the splash spreads farther radially than the flat impact ($t = 3.64$ ms) and the seal time is an order of magnitude longer ($t = 15.68$ ms).

963 A14-15

As a result, the size of the air cavity pulled under the surface is much larger (inset images in figure 8*a*). The images from the camera looking at the underside of the disk provide more insight into the differences between these two cases (figure 8*d* and supplementary movies 8 and 9). For flatter impact ($\alpha = 0.145°$), we see the trapped gas layer expected with disk impact ($t = 0.04$ ms) (Jain *et al.* 2021*a*). The layer breaks down as water contacts the impacting face in concentric rings ($t = 0.12$–0.56 ms), leaving a shrinking air pocket in the middle of the face ($t = 0.36$–1.52 ms). For the inclined impact ($\alpha = 0.44°$), the air layer mostly evacuates from beneath the impacting face prior to the face fully submerging. The air does not evacuate symmetrically (as indicated by the asymmetric wetting shown at $t = 0.12$ ms), rather it escapes beneath the inclined edge of the face. The escaping air then drives the asymmetric splash formation seen in the bottom sequence of figure 8(*c*). Any remaining air trapped beneath the disk collapses into small bubbles, rather than the contiguous pocket or rings of the smaller angle impact. Thus, an experimental deviation in α that one might intuitively have considered to be within 'measurement uncertainty' is indeed large enough to drastically change the splash and cavity behaviour for disk water impacts. We find that the angle has a similar, but less pronounced effect on cups (see Appendix A, figure 14). In the following section, we consider data from disk impacts for which the mean and standard deviation of α is $0.21°$ and $\pm0.11°$, respectively, for which we see the greatest similarity between disk and cup impact.

6. Cavity seal

The cavity seal is an important and well-documented phenomenon in water entry generally (Truscott *et al.* 2014). The time of the cavity seal t_{cs} marks the end of the process of cavity expansion as fed by the atmosphere above the free surface. As we have shown, this process contributes to the variety of regimes observed for cup impact. Figure 9(*a*) plots the dimensional cavity seal time t_{cs} for all cups as well as the disk; the cavity seal regimes are indicated by the marker shapes. The deep seal closure times are not affected by cup depth, nor are they sensitive to We_D. Plotting the normalized time $t_{cs}U/D$ against $Fr = U^2/gD$ for deep seal only (figure 9*b*) yields the same dependence of $t_{cs}U/D \propto Fr^{1/2}$ as for sphere water entry deep seal (Duclaux *et al.* 2007; Aristoff & Bush 2009). On the other extreme, the cavity seal time for closed torus cases is nearly two orders of magnitude faster than for deep seal (circle markers on figure 9*a*). The seal time in the closed torus regime is the time at which the wedge cavity seals, since the cavity does not reopen thereafter. Hypothesizing that the wedge seal is also a gravity-driven phenomenon, we plot $t_w U/r$ against $Fr_r = U^2/gr$ in figure 9(*c*). These data represent wedge seal times for all cases in which we have sufficient temporal and spatial resolution to identify the wedge seal (i.e. not just for closed torus events). The wedge seal event is indeed governed by gravity, and the data reveal a trend of $t_w U/r \propto Fr_r$.

As the cup regimes transition from deep seal to above-surface seal, the cavity seal times initially become very sensitive to We_D before plateauing as We_D increases (figure 9*a*). While the trends in the seal time curves are similar for all cup depths, the regime transitions from deep seal to above-surface seal occur at different values of We_D. By rescaling the data using We_r, we find that the transitions between these regimes align at $We_r \approx 2$, as shown in figure 9(*d*), which is consistent with the regime diagram in figure 3(*b*). The $h/D = 0$ data have also been rescaled using a length scale of 115 µm, which is of the order of the thickness of the trapped air layer for disk impacts as reported by Jain *et al.* (2021*a*). Whether the thickness of the trapped air layer or instead the machining radius on the edge of the cylinder is a more relevant length scale is not clear and is not pursued here.
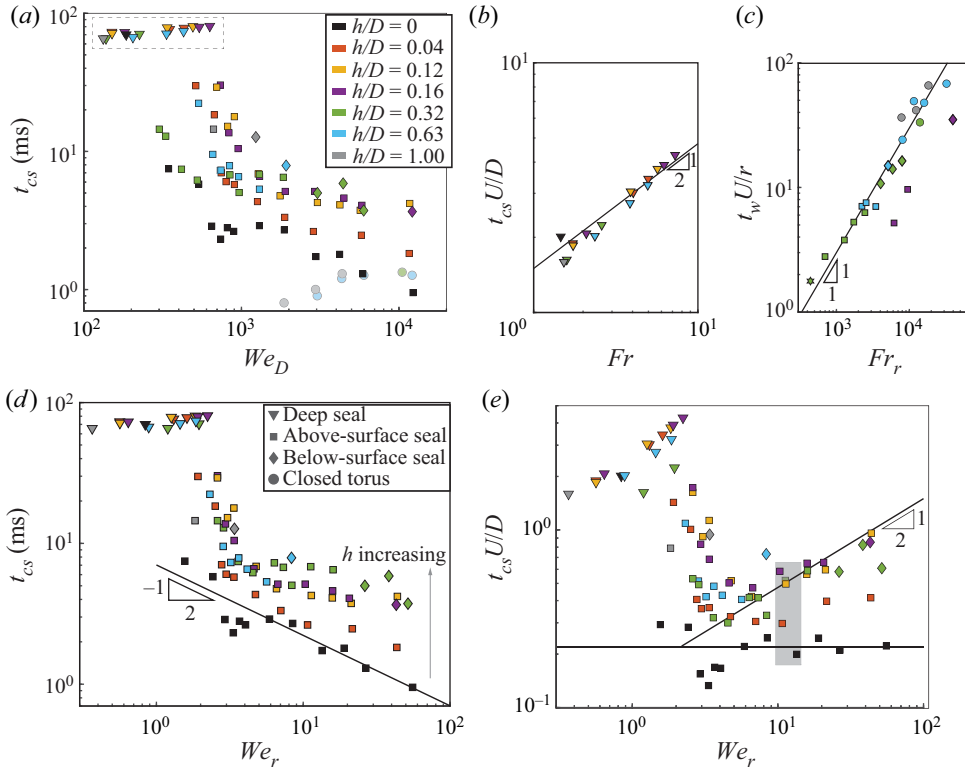
963 A14-16

Figure 9. Cavity seal time for cups and disks. (*a*) Seal time is constant for deep seal cases (outlined by dashed box) and then decreases with increasing We_D for other regimes. Seal time is consistently longer for cups than for disks, except for the closed torus regime. (*b*) In the deep seal regime, all bodies follow the scaling $t_{cs}U/D \propto Fr^{1/2}$, with the constant of proportionality equal to 1.5. (*c*) The wedge seal time scales with Froude, $t_w U/r \propto Fr_r$, where we use r as the length scale for normalization (proportionality constant on plot equals 3×10^{-3}.) (*d*) Re-scaling the data against We_r aligns the transition between deep seal and above-surface seal at $We_r \approx 2$. (*e*) Normalizing the seal time, we find that $t_{cs}U/D$ is constant for disks ($h/D = 0$) and $t_{cs}U/D \propto We_r^{1/2}$ as cup depth increases, for above-surface seal cases. The cases in the grey rectangle are discussed in figure 10. Marker colour indicates h/D, per the legend in panel (*a*). Marker shape indicates seal regime, per the legend in panel (*d*).

Normalizing the seal time, we find that $t_{cs}U/D$ is constant for the disk impacts in the above-surface seal regime (figure 9*e*). For sphere water entry in the same We_D range ($2 \times 10^3 - 3 \times 10^4$), Gilbarg & Anderson (1948) and Kiyama *et al.* (2022) also found that $t_{cs}U/D$ is constant. Eshraghi *et al.* (2020) rationalized this behaviour for spheres with a scaling analysis that balanced the radial splash rim inertia with the Bernoulli-induced pressure difference across the splash curtain that drives it to seal. We can conclude that the same phenomena are governing the cavity seal for disk impacts with $We_D \gtrsim 10^3$ ($We_r \gtrsim 3$) herein.

The dependence of above-surface seal time on cup depth becomes apparent for $We_r \gtrsim 3$. In the normalized plot of figure 9(*e*) as h/D increases, the seal time for cups follows the trend $t_{cs}U/D \propto We_r^{1/2}$. Thus, for the cases that follow this trend, $t_{cs} \neq f(U)$. However, the shallowest cup with $h/D = 0.04$ appears to follow a trend in between $t_{cs}U/D$ is constant and $t_{cs}U/D \propto We_r^{1/2}$. Furthermore, we observe that for different cups at the same impact
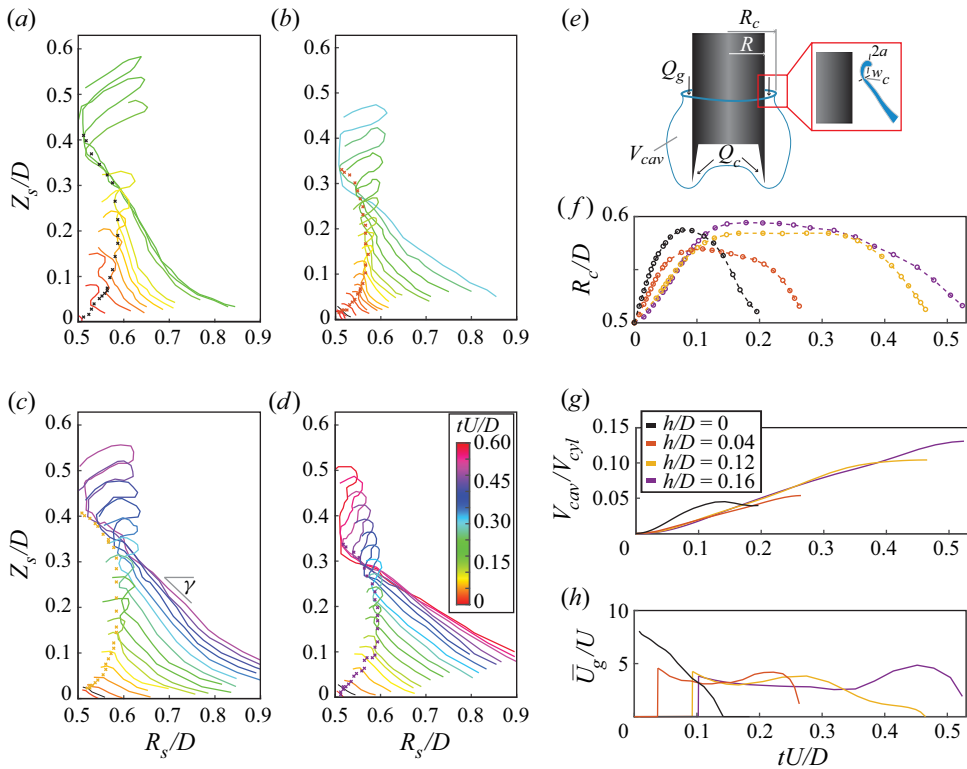
Figure 10. Radial (R_s) and vertical (Z_s) position of the splash over time for: (*a*) $h/D = 0$, $We_D = 2973$; (*b*) $h/D = 0.04$, $We_D = 2863$; (*c*) $h/D = 0.12$, $We_D = 3035$; and (*d*) $h/D = 0.16$, $We_D = 2913$. Splash contours are coloured by normalized time, tU/D. (*e*) Schematic of the two sources of gas flow into the cavity: from the cup (Q_c) and from the atmosphere (Q_g). The inset shows the definition of the splash rim with radius a and splash curtain with thickness w. The rim meets the splash curtain at point c, which is plotted with 'x-markers' on the plots in panels (*a*–*d*). (*f*) Radial position of point c, R_c, for the cases shown in panels (*a*–*d*). (*g*) Cavity volume over time, V_{cav}/V_{cyl}, where V_{cyl} is the total test body volume. (*h*) Gas flow velocity into the cavity $\overline{U}_g$ computed from (6.4).

speed (such as those highlighted by the grey box in figure 9*e*), as cup depth increases from $h/D = 0 \rightarrow 0.16$, cavity seal time t_{cs} also increases (as does $t_{cs}U/D$).

To better understand these observed differences in above-surface seal time between the different cups and the disk, we look further at the splash dynamics. Figure 10(*a*–*d*) show traces of the exterior surface of the splash over time for four of the cases highlighted by the grey box in figure 9*e* ($h/D = 0, 0.04, 0.12, 0.16$), which all have approximately the same Weber number ($We_D \approx 3000$, $We_r \approx 10$). The splash traces are coloured by tU/D, revealing that the splash for the disks rises up and closes in on the body more rapidly than for the cups. With increasing cup depth, the splash rises slower. The angle of the splash curtain γ also becomes shallower with increasing cup depth. This is due to the increased volume of escaping gas from the cup, which inflates the cavity below the free surface thereby displacing it upwards. The general features of the splash are consistent among the different impacting noses, and are characterized by a rim with radius a that sits atop an elongating sheet that meets the splash curtain at the point c (figure 10*e*). Point c is the first location on the splash to contact the body, and we plot its radial location over time for all

963 A14-18

h/D	U (m s^{-1})	a (μm)	$\dot{R}_{c_o}/U$
0	2.92	250	1.92
0.04	2.87	250	1.30
0.12	2.95	300	0.86
0.16	2.89	410	0.72

Table 1. Parameters for the four cases shown in figure 10.

four splashes in figure 10(*f*). The rim follows a roughly parabolic profile for the disk, but the trajectories for the cup cases are all broadened in time.

We seek to identify the possible mechanisms responsible for the differences in the splash development and seal time. Following Eshraghi *et al.* (2020), we use a simplified equation of motion for the splash curtain, whereby the curtain mass is accelerated towards the central axis by the gas velocity into the cavity,

$$m_c \frac{\mathrm{d}^2 R_c(t)}{\mathrm{d}t^2} = -\frac{1}{2} \rho_g A (\overline{U}_g(t))^2, \tag{6.1}$$

where $m_c \approx \rho w A$ is the splash curtain mass, R_c the radial position of the curtain, A the splash curtain surface area, w the curtain thickness, ρ_g the gas density and $\overline{U}_g(t)$ the mean gas flow velocity into the cavity. Equation (6.1) assumes that the air-flow-induced pressure difference across the splash curtain is the dominant force, which is a reasonable assumption for these impact speeds (Lee 2000; Eshraghi *et al.* 2020; Kiyama *et al.* 2022). Simplifying (6.1) gives

$$\frac{\mathrm{d}^2 R_c(t)}{\mathrm{d}t^2} = -\frac{\rho_g}{\rho} \frac{1}{2w} (\overline{U}_g(t))^2. \tag{6.2}$$

Splash curtain thickness (i.e. mass) can be inferred from measurements of the splash rim radius from images; that is, $w \sim a$ (see figure 10*e*, inset). Measurements of a are reported in table 1. The gas flow velocity can be related to the rate of change of cavity volume V_{cav} as

$$\frac{\mathrm{d}V_{cav}}{\mathrm{d}t} = Q_g + Q_c, \tag{6.3}$$

where Q_c is the flow rate of gas escaping from the cup into the cavity and $Q_g = \overline{U}_g(t)A_c(t)$ is the gas flow rate of air from the atmosphere into the cavity. This gas enters the cavity through the annular area $A_c(t)$ between the splash rim and the body, where $A_c(t) = \pi(R_c(t)^2 - R^2)$. Making these substitutions and rearranging (6.3) gives

$$\overline{U}_g(t) = \frac{1}{\pi(R_c(t)^2 - R^2)} \left[\frac{\mathrm{d}V_{cav}}{\mathrm{d}t} - Q_c \right]. \tag{6.4}$$

The rate of change $\mathrm{d}V_{cav}/\mathrm{d}t$ is estimated from measurements of V_{cav} from high-speed images, which are shown in figure 10(*g*) for the four cases under consideration. The cavity volume increases at approximately the same rate for the cup impacts, but increases more rapidly for the disk impact. Evaluating (6.4) for the disk case, with $Q_c = 0$ by definition and $R_c(t)$ measured (figure 10*f*), gives the estimates of $\overline{U}_g(t)$ plotted in figure 10(*h*). For the cups, we assume that $\mathrm{d}V_{cav}/\mathrm{d}t \approx Q_c$ from time $t = 0$ to $t = t_e + \tau$ (where $\tau = 0.4h/U$, see § 4.4), and $Q_c \approx 0$ thereafter. In other words, the cavity expansion is driven

963 A14-19

by gas escaping the cup at early times after impact, and then the cavity expansion is largely due to gas entering from the atmosphere, which induces the pressure difference across the splash curtain driving it to seal. We make this assumption based on observations of the gas escape process described in § 3. The ratio $\overline{U}_g/U$ is initially larger for the disk, while the cups maintain approximately the same (lower) constant gas flow velocity throughout the impact event. Furthermore, the delay time $t_e + \tau$ increases with increasing h/D.

Based on the above analysis, we conclude that two mechanisms are responsible for the faster cavity seal time observed for the disk and for cups with decreasing h for a given impact Weber number. First, the thickness of the splash curtain $w \sim a$ decreases as $h/D \to 0$, thus decreasing the mass of the splash per unit area (see table 1). We attribute this to the larger initial outwards radial velocity of the splash $\dot{R}_{c_o}$ as $h/D \to 0$, as seen in figure 10(f) and reported in table 1. The second mechanism driving faster seal time is the higher average gas flow velocity into the cavity, which results in a larger pressure difference across the splash curtain. The large rate of cavity expansion for the disk impact requires a higher gas flow velocity into the cavity. Not only is U_g smaller for cup impact, but gas inflow (and thus the pressure force on the curtain) is delayed due to the escape of trapped gas from the cup. This delay time increases as cup depth increases, which appears to contribute to the longer seal times for cups $h/D = 0.12$ and 0.16. A modelling approach would be required to tease out and confirm the relative importance of each mechanism; such a model is beyond the scope of this work. Nonetheless, our experimental measurements combined with a simple model of cavity seal (6.2) indicate that cups in the above-surface seal regime prolong cavity seal by generating a splash curtain with larger thickness and also by delaying and slowing the flow rate of atmospheric gas into the cavity. Therefore, in contrast with the cavity suppression induced by cups in the closed torus regime, cups in the above-surface seal regime actually promote cavity growth by delaying seal time relative to a disk.

7. Conclusions

We have shown that the water entry of cups can produce a variety of regime behaviours. These regimes are characterized by differences in the shape and size of the sub-surface gas cavity, as well as the evolution of the above-surface splash. We found several phenomena that persist for cup water entry over a range of dimensionless cup depths and Weber numbers. These include the formation and rapid closure of a wedge cavity that forms off the wedged cup walls, the escape of trapped gas from the cup and a possible reopening of the cavity to the air above. We proposed models for the cup gas dynamics in the limit of low and high Weber number, and these models accurately describe the experimental observations, including predicting the boundary of the closed torus regime. We found that cups can produce two divergent behaviours – cavity suppression or cavity enhancement – depending on cup depth and impact speed. Cavity suppression occurs when the cup is sufficiently deep so as to delay the time of gas escape such that the cavity never reopens to the air above. In cases in which the wedge cavity is reopened by the escaping gas, the seal time is longer than for disks. We deduced this to be due to a thicker splash sheet and slower gas flow velocity into the cavity, which reduces the pressure difference that drives the splash to seal. Our results extend understanding of the role of trapped gas on the water entry of rigid bodies, showing the dramatic effect it has on cavity and splash phenomena.

Declaration of interests. The authors report no conflict of interest.

Author ORCIDs.

Jesse Belden https://orcid.org/0000-0003-3754-6528;

Nathan B. Speirs https://orcid.org/0000-0003-4863-3993;

Tadd T. Truscott https://orcid.org/0000-0003-1613-6052.

Appendix A

A.1. *High-We_D model details*

Figure 11 shows a representative example of the predicted motion of the internal gas–liquid interface from the high-We_D model of § 4.2. The parameters for the cup impact are: $h = 4$ mm, $U_o = 4$ m s^{-1}. The interface starts at $x/h = 1$ and then the gas compresses and relaxes with decaying amplitude. The time to complete the first oscillation cycle is used as a prediction of the gas escape time t_e, as shown in figure 11.

The empirical constant κ in (4.14) is found by varying κ between 0 and 1 and plotting the closed torus boundary defined by (4.14) on the cavity and splash regime diagram. The results for several values of κ are shown in figure 12(a), from which we determine that $\kappa = 0.4$ best defines the closed torus boundary. Furthermore, to show that gas escape time t_e has a significant effect in defining the closed torus boundary, figure 12(b) plots the boundary given by (4.14) with t_e set to 0. Doing so fails to capture the observed dependence of the boundary on We_D.
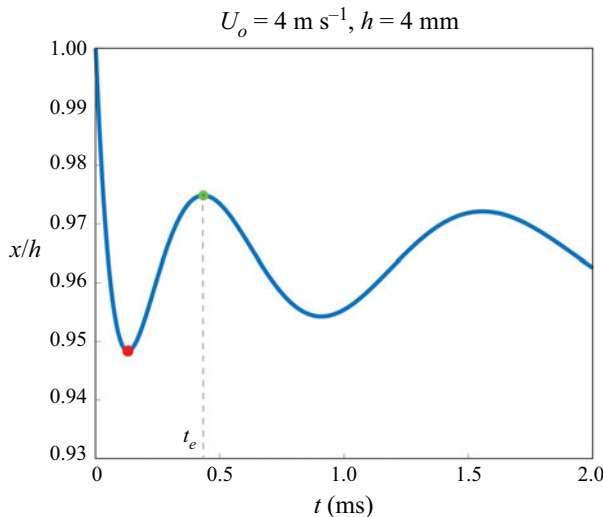

Figure 11. Prediction of the motion of the internal gas–liquid interface (x/h) versus time for a cup impact with parameters: $h = 4$ mm, $U_o = 4$ m s^{-1}. The interface motion is modelled using the high-We_D model of § 4.2.
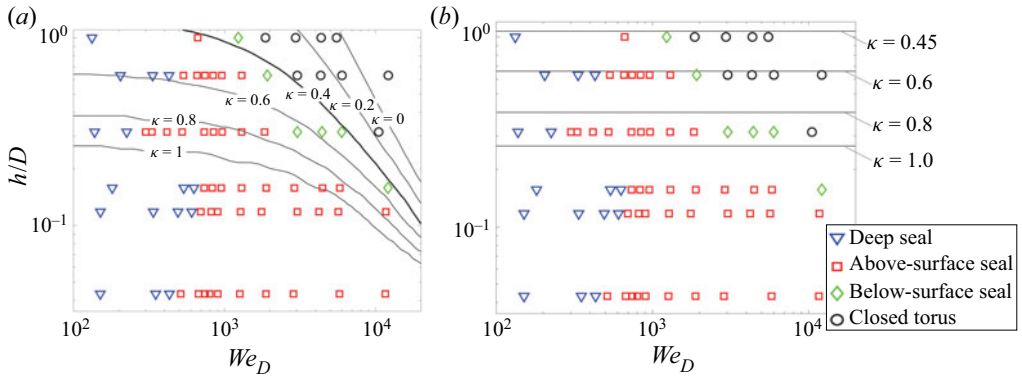
Figure 12. (*a*) Cavity and splash regime diagram with different curves for the closed torus boundary given by (4.14) for different values of κ. (*b*) Setting $t_e = 0$ fails to capture the observed dependence of the boundary on We_D.
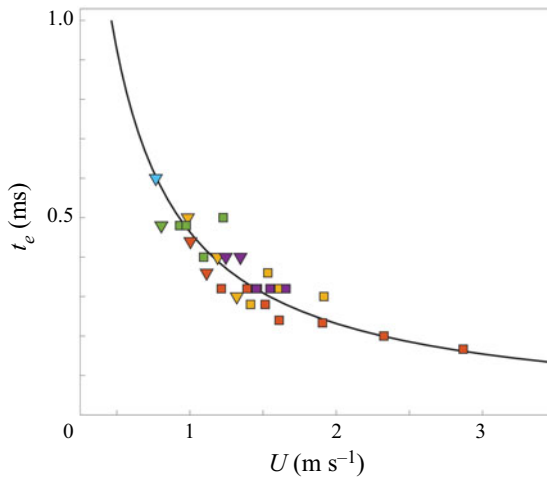

Figure 13. Gas escape time t_e as a function of impact speed U for cases with $We_D < We_{D_{crit}}$ as defined in figure 6(*c*). The black curve comes from (4.13) with $\kappa_l = 1.1(10^{-3})$.

A.2. *Low-We_D scaling analysis details*

The low-We_D scaling analysis results in (4.12). Because the low-We_D data do not show a dependence of t_e on h for a given We_D, we concluded that $l = \kappa_l h \propto h$, where κ_l is an empirical constant. This conclusion is further supported by figure 13, which plots t_e as a function of impact speed U for cases with $We_D < We_{D_{crit}}$ as defined in figure 6(*c*). The black curve comes from (4.13) with $\kappa_l = 1.1(10^{-3})$, showing good agreement with the data. Thus, even though two length scales (h and l) do appear in the scaling analysis, the data indicate that the gas escape time does not depend on h, at least for the parameter space explored herein. The appearance that t_e scales with $We_D^{-1/2}$ in figure 6(*a*) is actually a reflection that t_e scales with U^{-1}.
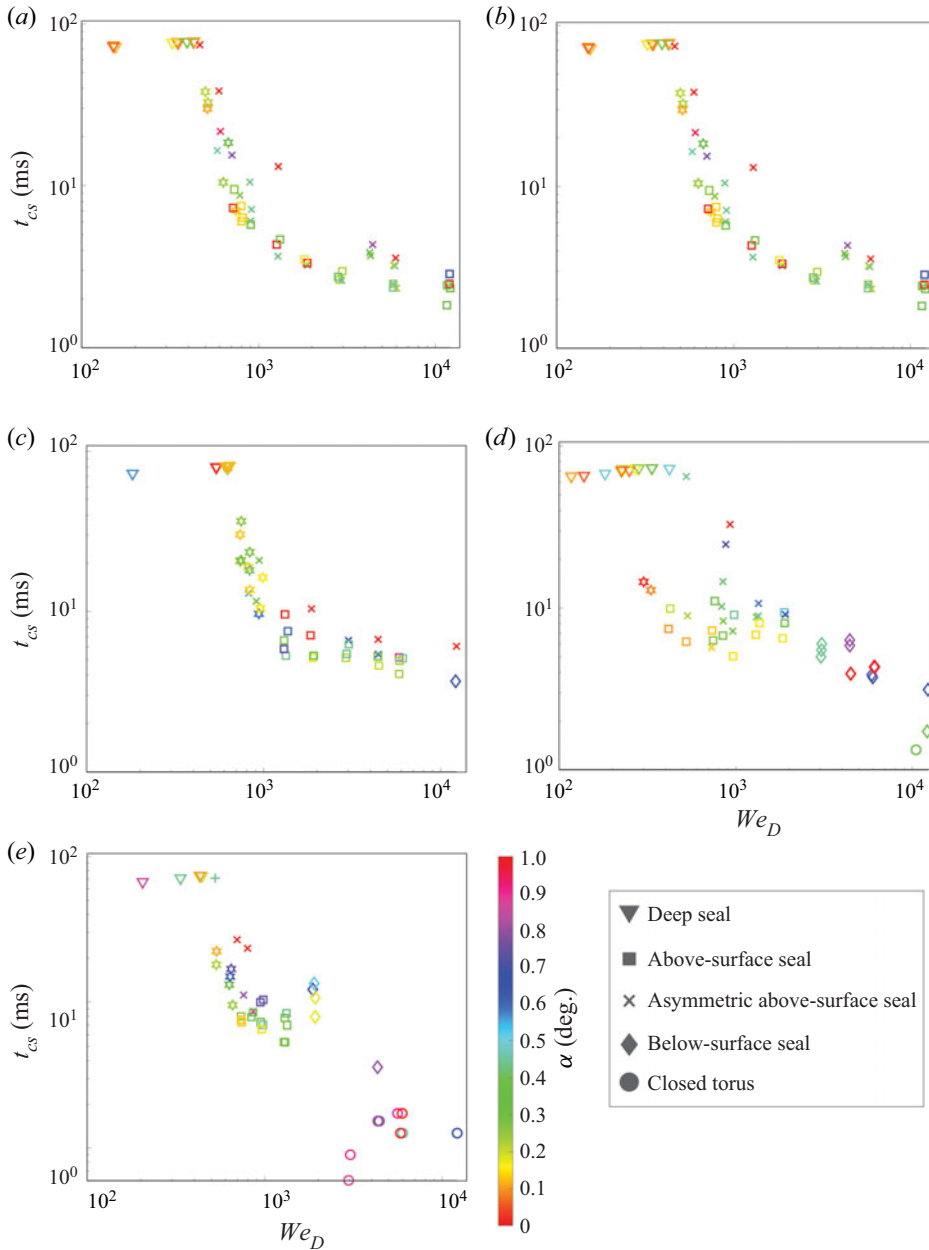
963 A14-22

Figure 14. Cavity seal time t_{cs} as a function of We_D for cups with: (*a*) $h/D = 0.04$; (*b*) $h/D = 0.12$; (*c*) $h/D = 0.16$; (*d*) $h/D = 0.32$ and (*e*) $h/D = 0.63$. The symbol colour indicates angle of attack α and the shape indicates the regime.

A.3. *Effect of impact angle on cup regimes*

Figure 14 plots the cavity seal time t_{cs} as a function of We_D for five different cup depths at all values of α measured in the experiment. In general, we find that t_{cs} is less sensitive to α for cups than it is for disks.

REFERENCES

ARISTOFF, J.M. & BUSH, J.W.M. 2009 Water entry of small hydrophobic spheres. *J. Fluid Mech.* **619**, 45–78.

BAGNOLD, R.A. 1939 Interim report on wave-pressure research (includes plates and photographs). *J. Inst. Civil Engrs* **12** (7), 202–226.

BERGMANN, R., VAN DER MEER, D., GEKLE, S., VAN DER BOS, A. & LOHSE, D. 2009 Controlled impact of a disk on a water surface: cavity dynamics. *J. Fluid Mech.* **633**, 381–409.

BODILY, K.G., CARLSON, S.J. & TRUSCOTT, T.T. 2014 The water entry of slender axisymmetric bodies. *Phys. Fluids* **26** (7), 072108.

DUCLAUX, V., CAILLÉ, F., DUEZ, C., YBERT, C., BOCQUET, L. & CLANET, C. 2007 Dynamics of transient cavities. *J. Fluid Mech.* **591**, 1–19.

DUEZ, C., YBERT, C., CLANET, C. & BOCQUET, L. 2007 Making a splash with water repellency. *Nat. Phys.* **3** (3), 180–183.

ESHRAGHI, J., JUNG, S. & VLACHOS, P.P 2020 To seal or not to seal: the closure dynamics of a splash curtain. *Phys. Rev. Fluids* **5** (10), 104001.

GILBARG, D. & ANDERSON, R.A. 1948 Influence of atmospheric pressure on the phenomena accompnaying the entry of spheres into water. *J. Appl. Phys.* **19**, 127–139.

JAIN, U., GAUTHIER, A.ïS, LOHSE, D. & VAN DER MEER, D. 2021*a* Air-cushioning effect and Kelvin–Helmholtz instability before the slamming of a disk on water. *Phys. Rev. Fluids* **6** (4), L042001.

JAIN, U., VEGA-MARTÍNEZ, P. & VAN DER MEER, D. 2021*b* Air entrapment and its effect on pressure impulses in the slamming of a flat disc on water. *J. Fluid Mech.* **928**, A31.

KIYAMA, A., RABBI, R., SPEIRS, N., BELDEN, J., TAGAWA, Y. & TRUSCOTT, T.T 2022 The water entry surface seal behavior of spheres at intermediate speed regimes. arXiv:2202.06342.

LEE, M. 2000 Water-entry induced cavity pressure. *KSME Intl J.* **14** (5), 562–568.

MANSOOR, M.M., MARSTON, J.O., VAKARELSKI, I.U. & THORODDSEN, S.T. 2014 Water entry without surface seal: extended cavity formation. *J. Fluid Mech.* **743**, 295–326.

MARSTON, J.O., TRUSCOTT, T.T., SPEIRS, N.B., MANSOOR, M.M. & THORODDSEN, S.T. 2016 Crown sealing and buckling instability during water entry of spheres. *J. Fluid Mech.* **794**, 506–529.

MATHAI, V., GOVARDHAN, R.N & ARAKERI, V.H 2015 On the impact of a concave nosed axisymmetric body on a free surface. *Appl. Phys. Lett.* **106** (6), 064101.

MAY, A. 1975 Water entry and the cavity-running behavior of missiles. *Tech. Rep*. NAVSEA Hydroballistics Advisory Committee Silver Spring Md.

PETERS, I.R, VAN DER MEER, D. & GORDILLO, J.M. 2013 Splash wave and crown breakup after disc impact on a liquid surface. *J. Fluid Mech.* **724**, 553–580.

SHIFFMAN, N & SPENCER, D.C. 1945 The force of impact on a sphere striking a water surface. *Tech. Rep*. AMG-NYU-133. New York University.

SPEIRS, N.B, MANSOOR, M.M, BELDEN, J. & TRUSCOTT, T.T 2019 Water entry of spheres with various contact angles. *J. Fluid Mech.* **862**, R3.

SUN, T., SHI, C., ZHANG, G., ZONG, Z. & WANG, H. 2021 Experimental study on the influence of the angle of attack on cavity evolution and surface load in the water entry of a cylinder. *Ocean Engng* **219**, 108271.

TRUSCOTT, T.T., EPPS, B.P. & BELDEN, J. 2014 Water entry of projectiles. *Annu. Rev. Fluid Mech.* **46** (1), 355–378.

YARIN, A.L. 2006 Drop impact dynamics: splashing, spreading, receding, bouncing. *Annu. Rev. Fluid Mech.* **38**, 159–192.

ZHANG, L.V., TOOLE, J., FEZZAA, K. & DEEGAN, R.D. 2012 Evolution of the ejecta sheet from the impact of a drop with a deep pool. *J. Fluid Mech.* **690**, 5–15.